https://doi.org/10.5194/wes-2025-52
Preprint. Discussion started: 8 April 2025

eawe european academy of wind energy
Open Access WIND ENERGY SCIENCE DISCUSSIONS

Wind turbine wake dynamics subjected to atmospheric gravity waves: A measurement-driven large-eddy simulation study

Dachuan Feng[1] and Simon Watson[1]

[1]Faculty of Aerospace Engineering, Delft University of Technology, 2629 HS Delft, the Netherlands

Correspondence: Dachuan Feng (D.Feng@tudelft.nl) and Simon Watson (S.J.Watson@tudelft.nl)

Abstract. Atmospheric gravity waves (AGWs) are large-scale wave-like flow structures commonly generated when atmospheric flows are vertically displaced by topography. These transient phenomena can significantly affect wind turbine outputs and loads; however, their influence on wake dynamics remains poorly understood, posing challenges for accurate wind farm modeling. In this study, we perform large-eddy simulation of wind turbines operating under an atmospheric condition reconstructed by assimilating lidar measurements of AGWs. Our results show that: (i) Low-frequency wake meandering becomes more pronounced owing to large-scale AGW flow structures and intensified smaller-scale turbulent structures. This enhanced meandering, combined with stronger turbulent mixing, accelerates mean wake recovery. (ii) Turbulence kinetic energy (TKE) spectrum in the wake region exhibits a peak Strouhal number of approximately 0.3, although the inflow spectrum peaks at significantly lower frequencies. This observation indicates that, under AGW conditions, wake turbulence generation follows a convective instability mechanism. Notably, faster wake recovery reduces wake shear, leading to lower amplification of TKE. Power analysis for three turbines arranged in a streamwise column further highlights the dominant role of convective instabilities. Large-amplitude, low-frequency power fluctuations observed at the most upstream turbine are significantly attenuated for downstream turbines, as low-frequency velocity fluctuations shift to higher frequencies in the far-wake regions. These findings add further insights into wake meandering and turbulence generation, offering guidance for modeling wind turbine and farm flows under non-stationary atmospheric conditions.

1 Introduction

Atmospheric gravity waves (AGWs) commonly occur when the atmosphere is vertically displaced by topographical features, such as mountains and coastlines (Nappo, 2012). These waves are trapped by the stable capping inversion layer aloft and propagate horizontally within the lowest 1-5 km of the troposphere (Durran, 2003). This transient phenomenon can cause fluctuations in wind speed experienced by wind farms, resulting in variations in power output and aerodynamic loading compared to conditions under mean synoptic forcing. In a wind farm, most turbines operate in the wake regions of upstream turbines. Therefore, understanding the response of turbine wakes to atmospheric phenomena, including AGWs, is critical for accurately modeling wind farm performance under realistic atmospheric conditions.

The influence of AGWs on wind farm performance has recently attracted considerable attention (Wilczak et al., 2019; Xia et al., 2021; Draxl et al., 2021). Through spectral analysis of field measurements and mesoscale simulations, researchers

https://doi.org/10.5194/wes-2025-52
Preprint. Discussion started: 8 April 2025

eawe european academy of wind energy
Open Access WIND ENERGY SCIENCE DISCUSSIONS

have observed that low-frequency oscillations in turbine and farm power production correlate with wind speed fluctuations associated with AGWs. More recently, Ollier and Watson (2022) conducted a parametric study using Reynolds-averaged Navier–Stokes simulations to investigate factors influencing AGW effects. Their findings highlight the importance of the wind farm's location within the wave cycle: wake losses in power production are mitigated during AGW peaks and exacerbated during AGW troughs.

Large-eddy simulation (LES) provides a robust method for generating detailed data on wind farm flows and outputs. To account for large-scale meteorological effects, mesoscale simulations (e.g., the Weather Research and Forecasting (WRF) model (Skamarock et al., 2008)) or field measurements (Allaerts et al., 2023; Quon, 2024) are often used to inform mesoscale forcing, which captures non-stationary atmospheric conditions such as diurnal thermal instability. Recently, Wise et al. (2024) combined LES with the WRF model to study interactions between AGWs and wind farms. Their results revealed that the passage of an AGW modulates the mesoscale environment, significantly impacting wind farm power production and structural loading.

Despite these advancements, several gaps remain. While prior studies have primarily focused on turbine outputs, the response of turbine wakes to AGWs remains poorly understood. Furthermore, it is unclear whether LES driven by field measurements can accurately capture transient atmospheric phenomena like AGWs. In this work, we use measurement-driven LES to explore the potential effects of AGWs on wake dynamics. Our analysis focuses on two key wake phenomena: (1) low-frequency meandering motions, which govern wake expansion and recovery, and (2) turbulence generation due to wake shear, which enhances turbulent kinetic energy (TKE) within the wake region.

We introduce the American WAKE experimeNt (AWAKEN) field campaign which provides measurements of AGWs and the measurement-driven LES setup in Sect. 2. Then, we analyze the effects of AGWs on wake meandering, wake turbulence generation, mean wake recovery, and power fluctuations in Sect. 3. Finally, we present our conclusions in Sect. 4.

2 Methods

2.1 AWAKEN measurement

AWAKEN is a large-scale field campaign designed to obtain detailed observations of wind farm–atmosphere interactions, with the goal of advancing the understanding of wind farm physics and improving overall performance (Moriarty et al., 2020). Figure 1 shows the schematic of the measurement sites and terrain features in the AWAKEN campaign. Given the prevailing southerly wind direction, site A1 serves as the inflow condition for the King Plains wind farm, which is the most instrumented wind farm. The west-east mountainous terrain in this region causes multiple AGW events, which have been identified from atmospheric measurements.

For this study, we focus on the AGW event on 8 June 2023, because its vertical extent spans the rotor layer of a wind turbine. Figure 2 shows the radar observations of this AGW event. The wind speed peaks and troughs elongated in the northwest-southeast direction indicate large-scale wave-like structures flowing over multiple wind farms. These wave-like structures horizontally propagate from southwest to northeast with a wavelength of approximately 2.5-3 km.

https://doi.org/10.5194/wes-2025-52
Preprint. Discussion started: 8 April 2025

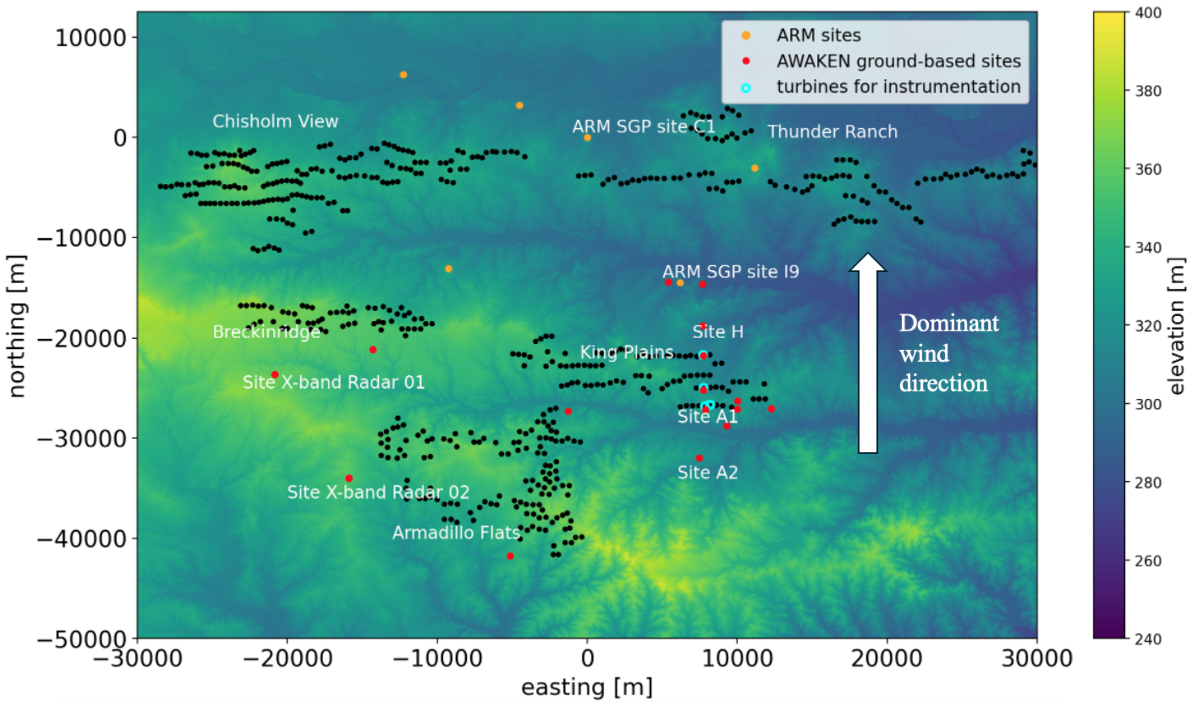

Figure 1. Map of AWAKEN measurement sites. The contour value is elevation over the sea level. The figure is adapted from Debnath et al. (2022). The white arrow indicates the prevailing southerly wind.

In Fig. 3, the top-left panel shows lidar measurements of wind speed at site A1 during the selected AGW event. The horizontal axis represents UTC time (local time + 5 hours), while the vertical axis represents height above ground level. The duration of the AGW event is approximately 1200 s and the wind speed exhibits low-frequency oscillations with a period of roughly 600 s. Missing observations near the ground have been filled using a natural neighbor interpolation technique (Allaerts et al., 2023), and the resulting fixed time–height history is shown in the bottom-left panel. It should be noted that although orographically-induced AGWs are theoretically stationary, this is only true for the component of the wave group velocity parallel to the background wind. This means that in practice the AGWs are advected by the background wind depending on its component perpendicular to the wave group velocity. In addition, horizontal shear in the background wind speed can contribute to horizontal advection by refracting the AGWs. The high-speed region at lower heights suggests the presence of a low-level jet. This vertical wind profile deviates significantly from the standard atmospheric boundary layer profile, where wind speed typically increases monotonically with height above the ground.

2.2 Measurement-driven LES

A measurement-driven large-eddy simulation (LES) model is developed to simulate turbine flow under AGW inflow conditions. This approach leverages the mesoscale-microscale coupling capability of SOWFA (Simulator for Wind Farm Applica-

https://doi.org/10.5194/wes-2025-52
Preprint. Discussion started: 8 April 2025

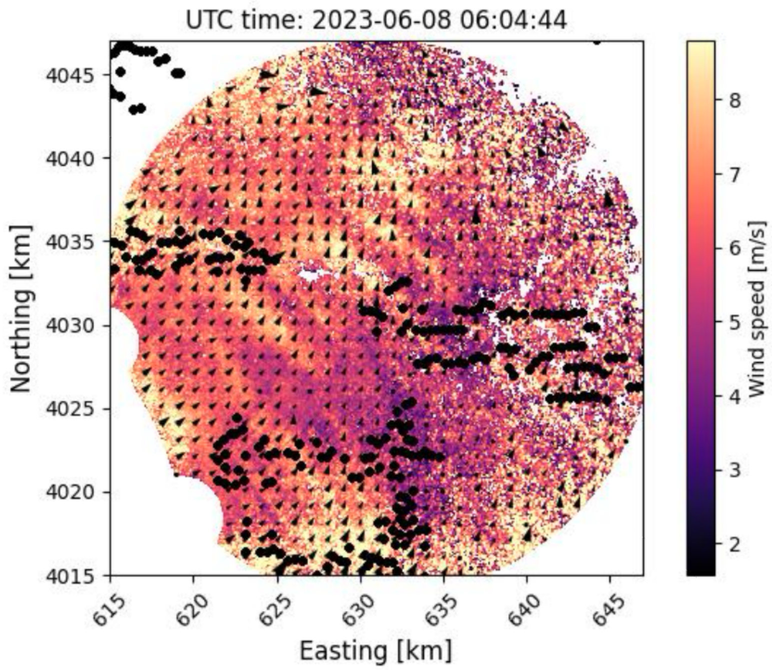

Figure 2. Radar measurement taken approximately at the hub height during the AGW event on 8 June 2023. The figure is provided by US National Renewable Energy Laboratory (NREL). Black solid circles represent wind turbines.

tions) (Churchfield et al., 2012) and the high spatio-temporal resolution measurements from the AWAKEN campaign. The simulation is carried out in two stages: (i) inflow simulation, which assimilates AGW measurements into the atmospheric simulation, and (ii) turbine simulation, which generates wind turbine wake flow under the measurement-assimilated inflow condition.

In the first stage, the inflow simulation solves the spatially filtered incompressible Navier–Stokes equations of mass and momentum, and the transportation equation of potential temperature. The momentum equation includes two source terms. One source term accounts for mesoscale forcing computed through an indirect profile assimilation method (Allaerts et al., 2020). This method ensures that the LES solution reproduces the time-height wind speed profile shown in the top panel of the bottom-left contour in Fig. 3, thus capturing the key characteristics of the AGW inflow. The other source term in the momentum equation accounts for the Coriolis force induced by planetary rotation. The potential temperature remains constant below the capping inversion layer and increases linearly in the above regions, which follows the potential temperature profile in conventionally neutral boundary layers. The inversion layer height is set as 1250 m, based on the vertical distribution of wind speed shown in the left column of Fig. 3. Subgrid-scale effects are modeled using a standard turbulent kinetic energy (TKE) equation (Deardorff, 1980).

The computational domain is configured as a straight channel with dimensions of $3000 \times 3000 \times 1500$ m in the streamwise, spanwise and vertical directions, respectively. The domain is discretized into $300 \times 300 \times 150$ grid cells. A slip-wall condition

https://doi.org/10.5194/wes-2025-52
Preprint. Discussion started: 8 April 2025

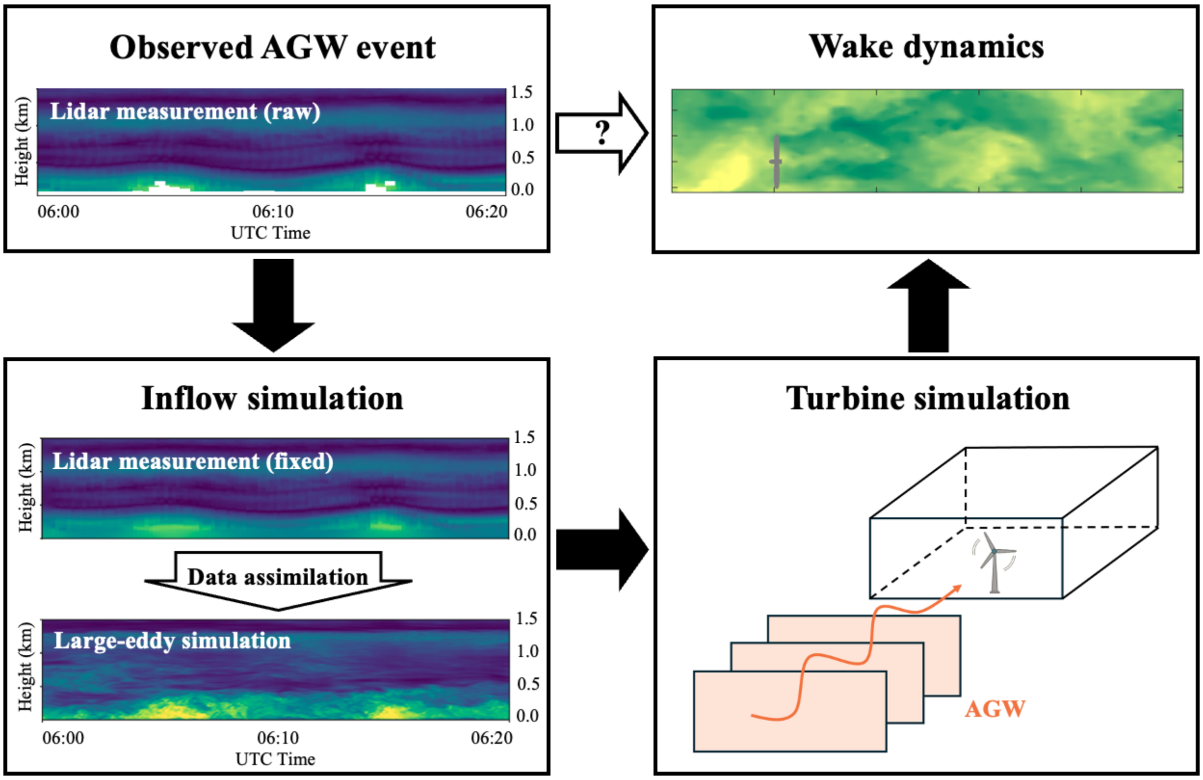

Figure 3. Flow chart of the present measurement-driven LES study. In the left column of contours, from blue to yellow indicates wind speed from 0 to 7.5 m/s. In top-right contour, from green to yellow indicates magnitudes from 0.2 to 1.4 for streamwise velocity normalized by inflow mean velocity at the hub height.

is applied at the upper boundary, with velocity gradients set to zero, while the bottom boundary uses a local-similarity-based logarithmic wall model (Moeng, 1984) to account for viscous and subgrid-scale stresses. The effective roughness height is set to 0.1 m, representing typical onshore terrain. Periodic conditions are applied at the lateral boundaries.

The inflow simulation runs for 2400 s, with the first 1200 s allocated for spin-up and the remaining 1200 s representing the AGW event. In the bottom-left contour of Fig. 3, the bottom panel displays the time-height wind speed history from the inflow simulation. When compared to the lidar measurements in the top panel, the present LES not only captures the low-frequency wind speed oscillations caused by the AGW event but also resolves turbulence structures with higher spatio-temporal resolution than can be captured by the lidar. The LES solution for velocity and temperature at the upstream boundary is saved at a time step of 0.5 s during the last 1200 s, providing inflow conditions for the subsequent turbine simulation. These inflow data are represented by the orange slices in the bottom-right of Fig. 3.

In the second stage, the turbine simulation incorporates the effect of wind turbines as additional source terms in the Navier–Stokes momentum equations. The turbine is modeled using the NREL 5-MW reference turbine (Jonkman, 2009), a three-bladed horizontal-axis turbine with a rotor diameter of $D = 126$ m and a hub height of 90 m. This open-source turbine model

https://doi.org/10.5194/wes-2025-52
Preprint. Discussion started: 8 April 2025

eawe european academy of wind energy
Open Access WIND ENERGY SCIENCE DISCUSSIONS

is used as a proxy for the 2.8-MW General Electric turbines deployed at the King Plains wind farm. The turbine is placed $5D$ downstream of the inflow boundary, and its forcing is modeled using an actuator disk method with rotation (Wu and Porté-Agel, 2011). While the effects of the nacelle and tower are neglected, this method has demonstrated good agreement with wind tunnel measurements and high-fidelity numerical simulations in the far wake region, which primarily influences wind farm flow characteristics. The turbine operates at a rotational speed of nine rotations-per-minute (9 rpm).

The inflow simulation slices are imposed at the inflow boundary. A Rayleigh damping layer is applied at the outflow boundary to prevent unphysical wave reflections. The remaining boundary conditions (top, bottom, and lateral) are consistent with those used in the precursor inflow simulation. After convergence, the flow field and turbine power are saved. The flow data collection subdomain spans $-2 \leq x/D \leq 8$, $-2 \leq y/D \leq 2$, and $-0.7 \leq z/D \leq 2$, where x, y, and z represent the streamwise, spanwise, and vertical coordinates, respectively. The origin is located at the turbine hub center.

The turbine simulation provides wake flow data which can be used to analyze the wake dynamics under the AGW inflow condition, referred to as the AGW case. For comparison, we also perform a turbine simulation without AGWs, referred to as the non-AGW case. In this case, a conventionally neutral boundary layer is simulated as the inflow condition using a wall-modeled LES method designed to capture scaling laws for both mean velocity and velocity fluctuations (Feng et al., 2024a). Once the inflow simulation reaches a statistically steady state, the flow data are collected for an additional 1200 s, as in the AGW case. Both the mean wind speed at the hub height, $U_{\mathrm{hub}} = 5$ m/s (consistent with the mean lidar measurements), and vertical temperature profile remain identical for the AGW and non-AGW inflow conditions. However, while the non-AGW inflow follows a logarithmic scaling law, the AGW inflow exhibits a jet-like shape in the vertical wind-speed profile.

Throughout this paper, the instantaneous streamwise, spanwise, and vertical velocity components are denoted as u, v and w with their time-averaged counterparts denoted as U, V and W. Time-averaging is performed over the 1200-s duration of the AGW event, which corresponds to approximately two wave cycles.

3 Results and discussions

3.1 Wake meandering

Wake meandering refers to large-scale oscillations of the wake flow driven by low-frequency spanwise and vertical velocity fluctuations in the atmospheric flow. These velocity fluctuations intermittently change the wind direction, causing the wake flow to deflect as if it were a passive tracer. Fig. 4 presents instantaneous velocity contours in the spanwise (top) and vertical (bottom) planes for both the AGW (left) and non-AGW (right) cases. The snapshot corresponds to the first peak in wind speed during the AGW event. In both planes, the AGW case causes larger-scale deflections of the wake center, indicative of stronger wake meandering, compared to the non-AGW case. As a result, the AGW case shows a greater range of wake excursions. Specifically, as shown in the left column of Fig. 4, both spanwise and vertical wake excursions extend beyond one rotor diameter for the AGW case, whereas for the non-AGW case, they only slightly exceed 0.5 turbine diameter.

To quantify the mean amplitude of wake meandering, we use a metric, A_{m}, defined as the standard deviation of large-scale wake-center deflections. The wake centers are determined by first filtering the instantaneous wake-deficit flow field with a

https://doi.org/10.5194/wes-2025-52
Preprint. Discussion started: 8 April 2025

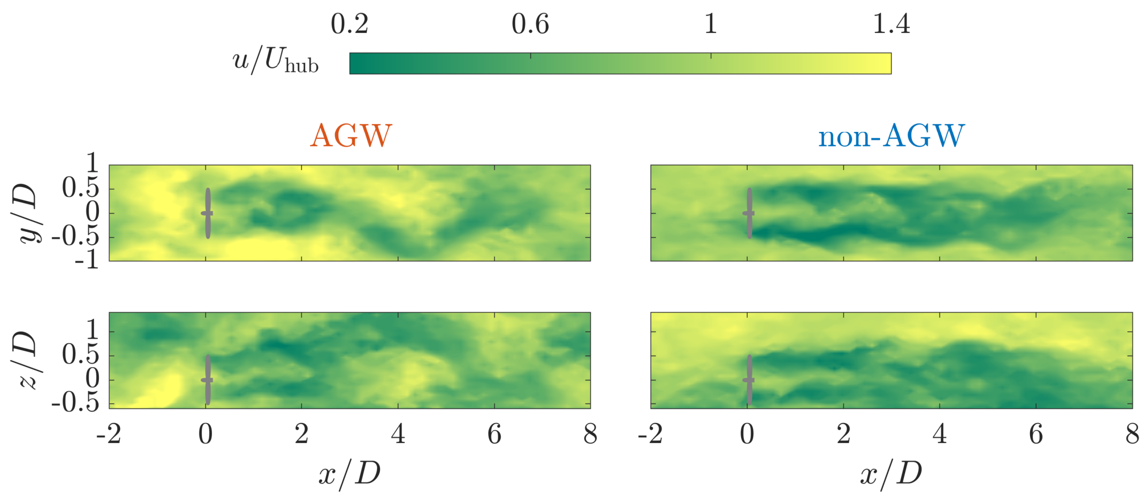

Figure 4. Instantaneous streamwise velocity normalized by U_{hub} in the spanwise (top) and (bottom) vertical planes passing through the turbine center. The data are compared between the AGW (left) and non-AGW (right) cases. The gray bar in each plot indicates the turbine location.

spatial filter spanning three rotor diameters to isolate meandering motions (Feng et al., 2022). The filtered wake deficit is then fitted to a two-dimensional Gaussian profile at each downstream location, following the method described by Trujillo et al. (2011). The location of the maximum wake deficit is taken as the wake center. Fig. 5 shows A_{m} in the far-wake region ($4 \leq x/D \leq 8$).The meandering amplitude generally increases with downstream distance, as the wake-center deflection at each downstream location is a cumulative effect of upstream deflections. In both the spanwise and vertical planes, the AGW case results in A_{m} nearly double that of the non-AGW case, consistent with the observations in Fig. 4.

The stronger wake meandering observed in the AGW case can be attributed to two primary factors: (i) Presence of AGW wavy structures: These large-scale flow structures induce low-frequency, large-magnitude velocity fluctuations in both the spanwise and vertical directions, thereby amplifying wake meandering magnitudes. (ii) Increased turbulence level: Turbulent structures with length scales larger than three rotor diameters can cause wake meandering. These structures become more pronounced when AGWs are present, further intensifying the meandering motion.

3.2 Wake turbulence generation

While wake meandering is driven by large-scale velocity fluctuations, wake turbulence is predominantly generated through convective instabilities associated with smaller-scale velocity fluctuations. The convective instability mechanism suggests that TKE generation in the wake arises from the selective amplification of upstream velocity fluctuations by shear instabilities induced by wake shear (Heisel et al., 2018; Foti et al., 2018; Feng et al., 2024b). The streamwise, spanwise and vertical velocity fluctuations are $u' = u - U$, $v' = v - V$ and $w' = w - W$, respectively. TKE is then calculated as $u'^2 + v'^2 + w'^2$.

https://doi.org/10.5194/wes-2025-52
Preprint. Discussion started: 8 April 2025

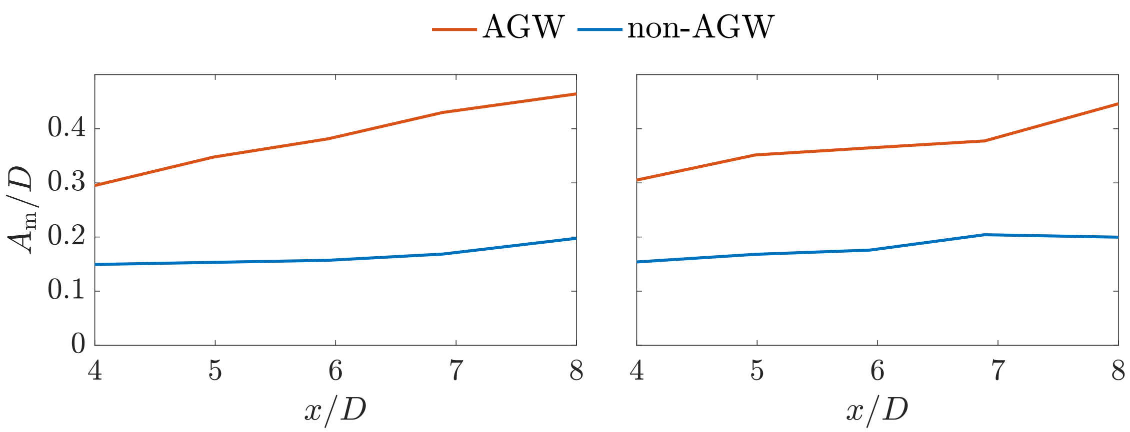

Figure 5. Mean magnitudes of wake meandering in the spanwise (left) and (right) vertical directions for distances $4D$-$8D$ downstream of the turbine. The data are compared between the AGW (red line) and non-AGW (blue line) cases.

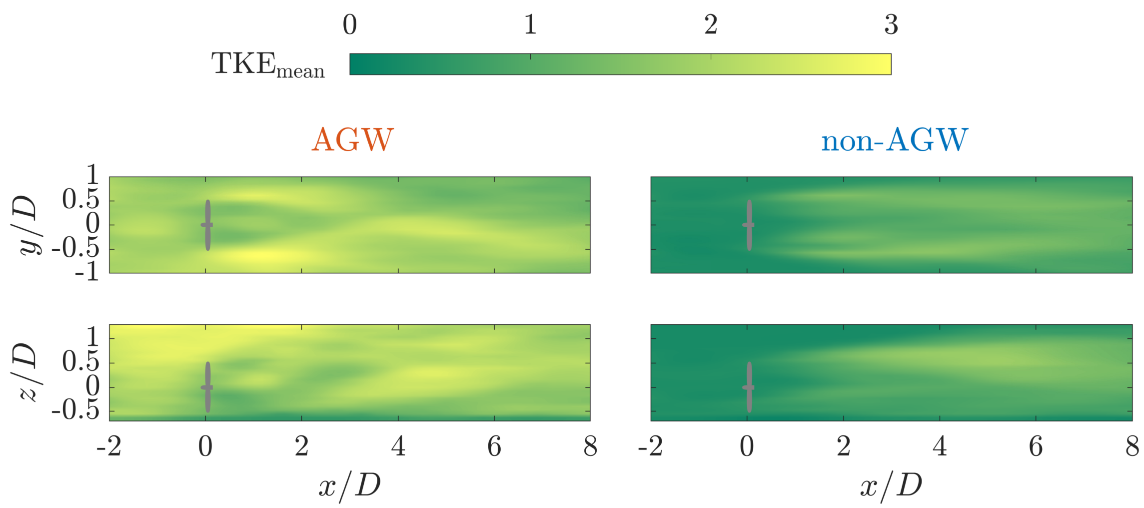

Figure 6. Mean TKE in the spanwise (top) and vertical (bottom) planes passing through the turbine center. The data are compared between AGW (left) and non-AGW (right) cases.

Figure 6 shows the time-averaged TKE in the spanwise (top) and vertical (bottom) planes for the AGW (left) and non-AGW (right) cases. Compared to the non-AGW case, the AGW case exhibits higher mean TKE levels in both the inflow and wake regions, but lower TKE generated in the wake region when normalized by the inflow TKE. Herein, we define a measure for
155 such inflow-normalized TKE generation as $\Delta\mathrm{TKE}^*_{\mathrm{mean}} = (\mathrm{TKE}_{\mathrm{mean}} - \mathrm{TKE}_{\mathrm{mean,in}})/\mathrm{TKE}_{\mathrm{mean,in}}$, where $\mathrm{TKE}_{\mathrm{mean,in}}$ is the mean TKE at $x/D = -2$. The TKE field is spatially-averaged over the rotor disk area at each streamwise location.

https://doi.org/10.5194/wes-2025-52
Preprint. Discussion started: 8 April 2025

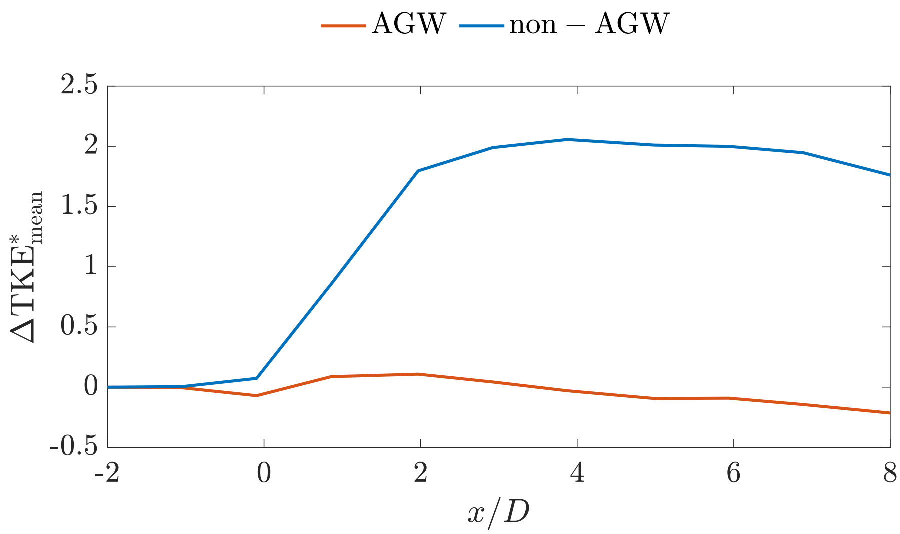

Figure 7. Inflow-normalized TKE generation, $\Delta\mathrm{TKE}^*_{\mathrm{mean}}$, at each streamwise location. The data are compared between the AGW (red line) and non-AGW (blue line) cases.

Figure 7 shows streamwise variation of $\Delta\mathrm{TKE}^*_{\mathrm{mean}}$ for the AGW and non-AGW cases. In the AGW case, $\Delta\mathrm{TKE}^*_{\mathrm{mean}}$ initially remains close to zero before slightly decreasing in the far-wake region. By contrast, in the non-AGW case, $\Delta\mathrm{TKE}^*_{\mathrm{mean}}$ increases sharply to approximately 2 and maintains similar values in the far-wake region, indicating that the wake TKE is nearly three times the inflow TKE. The significantly lower $\Delta\mathrm{TKE}^*_{\mathrm{mean}}$ in the AGW case can be attributed to reduced wake shear, which results from faster wake recovery, as we will discuss in Sect. 3.3.

To investigate the spectral characteristics of wake turbulence generation, we applied Fourier transforms to the time series of velocity fluctuations to compute the power spectral density of TKE, $\phi_{\mathrm{TKE}} = \phi_u + \phi_v + \phi_w$ (where ϕ_u, ϕ_v and ϕ_w represent the power spectral density of u', v' and w', respectively). Fig. 8 shows TKE spectra multiplied by frequency, $f\phi_{\mathrm{TKE}}$, at various Strouhal numbers, $St = fD/U_{\mathrm{hub}}$ (f is the frequency, D is the rotor diameter, and U_{hub} is the hub-height mean inflow wind speed), for the AGW (top) and non-AGW (bottom) cases. The area under the spectral curve corresponds to the TKE within a specific frequency range. The dotted and solid lines represent the spectra calculated for the inflow region ($2D$ upstream of the turbine) and the wake region ($4D$ downstream of the turbine), respectively.

Despite differences in the peak frequencies of inflow TKE, the wake TKE for both AGW and non-AGW cases is concentrated within a similar frequency range, $0.1 < St < 1$. The peak Strouhal number in the wake TKE spectra, $St_{\mathrm{wake}} \approx 0.3$, corresponds to the characteristic frequency of shear-induced wake turbulence. This frequency has been shown to be independent of turbine design and operating conditions (Foti et al., 2018; Heisel et al., 2018). Therefore, we conclude that the presence of AGWs does not alter the dominant role of convective instabilities in wake turbulence generation.

https://doi.org/10.5194/wes-2025-52
Preprint. Discussion started: 8 April 2025

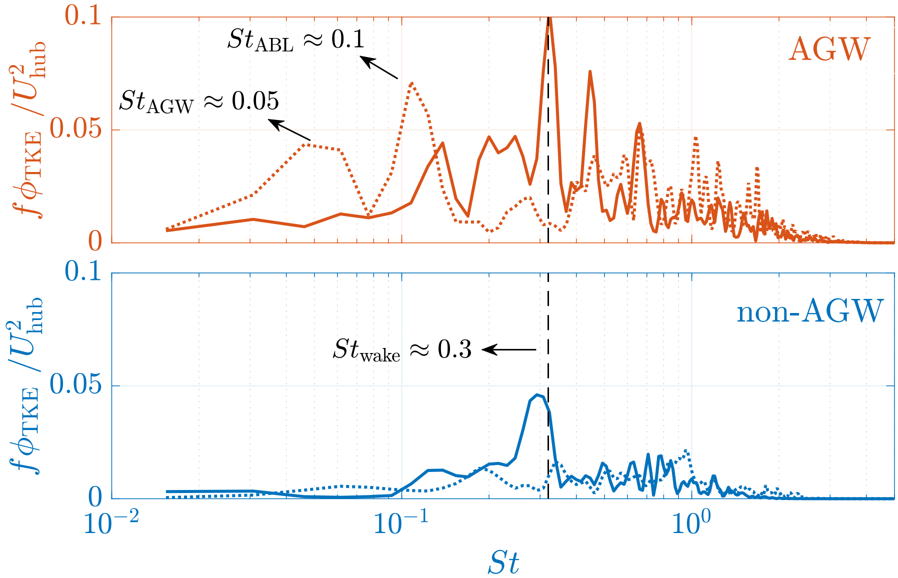

Figure 8. TKE spectra multiplied by the frequency f and non-dimensionalized by U_{hub}^2 as a function of Strouhal number $St = fD/U_{\mathrm{hub}}$. The data are compared between the AGW (top) and non-AGW (bottom) cases. In each plot, the dotted and solid lines represent spectra calculated at $(x/D, y/D, z/D) = (-2, 0, 0)$ for the inflow and $(x/D, y/D, z/D) = (4, 0, 0)$ for the wake, respectively.

While the mechanism of turbulence generation remains consistent, the AGW and non-AGW cases exhibit notable differences in their TKE spectra. For the AGW case (top panel of Fig. 8), the inflow spectrum reveals two distinct peaks: (i) A lower-frequency peak at $St_{\mathrm{AGW}} \approx 0.05$, corresponding to the AGW wavelength of approximately 2 km, highlighting the capability of the precursor inflow simulation to capture the AGW event; (ii) A higher-frequency peak at $St_{\mathrm{ABL}} \approx 0.1$ associated with the atmospheric boundary layer thickness of approximately 1250 m, as indicated by the inversion capping layer height in the top-left contour of Fig. 3. In the wake region, the TKE from these inflow peaks shifts to higher frequencies, $0.1 < St < 1$, with comparable magnitudes. In contrast, for the non-AGW case, the inflow TKE magnitudes are significantly amplified in the wake TKE spectra. This provides spectral evidence supporting the observation in Fig. 6, which shows that fractional TKE generation is higher in the non-AGW case.

3.3 Mean wake recovery

The expansion of the mean wake flow is driven by a combined effect of wake meandering and turbulent mixing in the instantaneous wake flow. Consequently, larger meandering amplitudes can lead to greater wake expansion and faster recovery. In this section, we analyze the characteristics of the mean wake flow to support the findings in Sect. 3.1, which suggest that AGWs enhance wake meandering.

https://doi.org/10.5194/wes-2025-52
Preprint. Discussion started: 8 April 2025

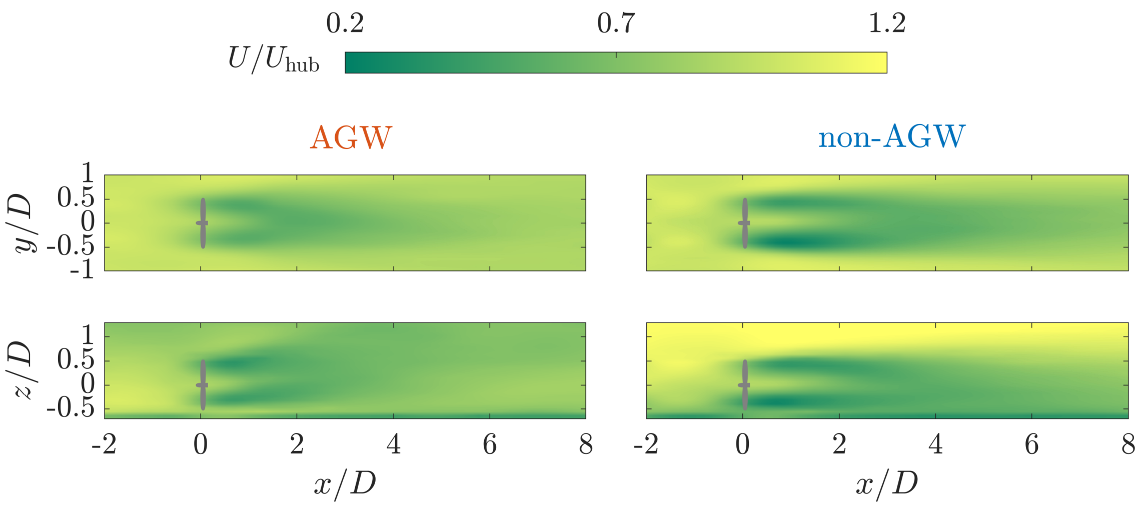

Figure 9. Mean streamwise velocity normalized by U_{hub} in the spanwise (top) and vertical (bottom) planes passing through the turbine center. The data are compared between AGW (left) and non-AGW (right) cases. The gray bar in each plot indicates the turbine location.

Fig. 9 shows time-averaged streamwise velocity contours in the spanwise (top) and vertical (bottom) planes for the AGW (left) and non-AGW (right) cases. The velocity magnitudes are normalized by U_{hub}. For all plots, the wake region ($0 \leq x/D \leq 8$) exhibits a velocity deficit compared to the inflow region ($-2 \leq x/D \leq 0$) as might be expected. However, in both the spanwise and vertical directions, the wake velocity recovers more quickly towards the ambient velocity for the AGW case. Additionally, as shown in the bottom row of Fig. 9, the AGW and non-AGW cases exhibit distinctly different vertical profiles in the inflow region. While the non-AGW inflow follows a standard boundary layer profile, the AGW inflow shows a low-level jet with the jet nose located near hub height. These low-level jets are also evident in the time-height wind speed history depicted in the left column of Fig. 3.

In order to provide a quantitative comparison, Fig. 10 shows the U_{hub}-normalized mean streamwise velocity along the turbine centerline in the wake region. In both the AGW and non-AGW cases, the velocity initially decreases as a result of the pressure recovery immediately behind the rotor and due to the speed-up region near the turbine center gradually diffusing due to momentum exchange. The velocity then begins to recover from approximately $x/D = 2$ or 3, where the wake deficit becomes Gaussian-shaped. At $x/D = 8$, the velocity recovers to approximately 90% of the ambient velocity for the AGW case, compared to around 75% for the non-AGW case.

The faster recovery of the mean wake in the AGW case can be attributed to two key factors: (i) Stronger wake meandering: The AGW inflow contains more intense large-scale turbulent structures, leading to greater meandering amplitudes and, consequently, larger mean wake expansion (Ainslie, 1988; Larsen et al., 2008). (ii) Higher turbulence levels: The presence of AGWs increases TKE, enhancing turbulent mixing in the wake region and accelerating velocity recovery.

https://doi.org/10.5194/wes-2025-52
Preprint. Discussion started: 8 April 2025

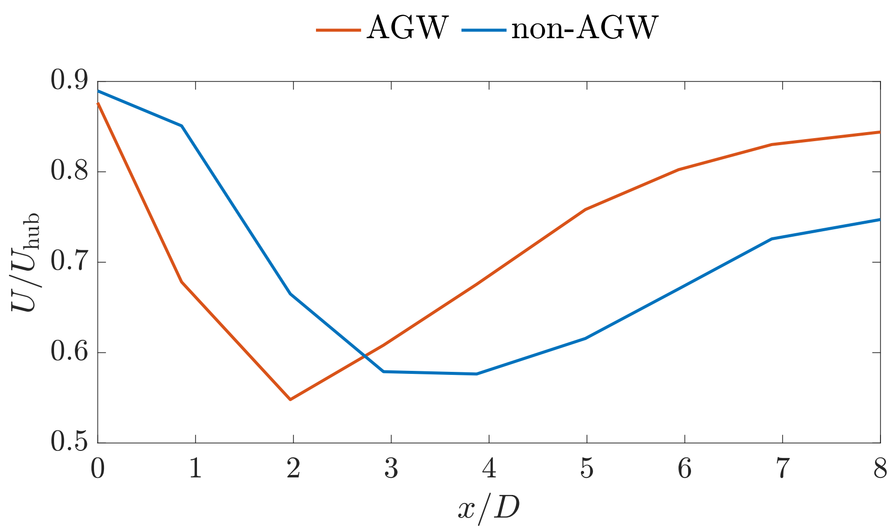

Figure 10. Mean streamwise wake deficit along the turbine centerline. The data are compared between the AGW (red line) and non-AGW (blue line) cases.

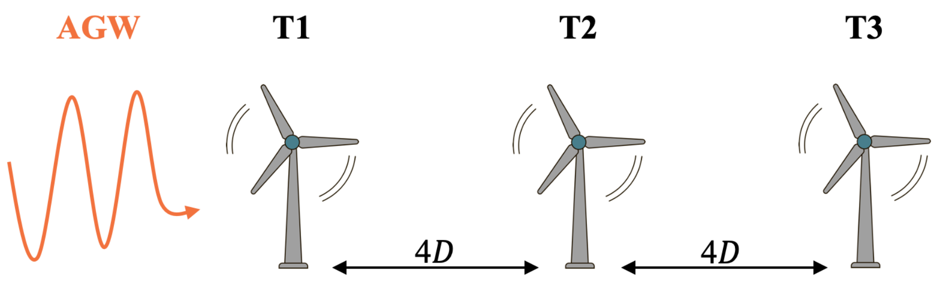

Figure 11. Schematic of the simulation of three turbines under the AGW inflow condition. From upstream to the downstream is subsequently T1, T2 and T3.

3.4 Power output of waked turbines

In this section, we analyze the power output of turbines operating in wake regions to validate the dominant role of convective instabilities in wake turbulence generation, as discussed in Sect. 3.2. We simulated three turbines–T1, T2, and T3–arranged in a streamwise column under AGW inflow conditions, as shown in Fig. 11. The turbines were spaced $4D$ apart, ensuring that the waked turbines (T2 and T3) operated at the same downstream distances where the wake spectra in Fig. 8 were computed.

Fig. 12 presents the time series of power fluctuations for the three turbines. For T1, large-magnitude, low-frequency power fluctuations (with peaks and troughs marked by red circles) are observed, driven by large-scale wind speed fluctuations in the

https://doi.org/10.5194/wes-2025-52
Preprint. Discussion started: 8 April 2025

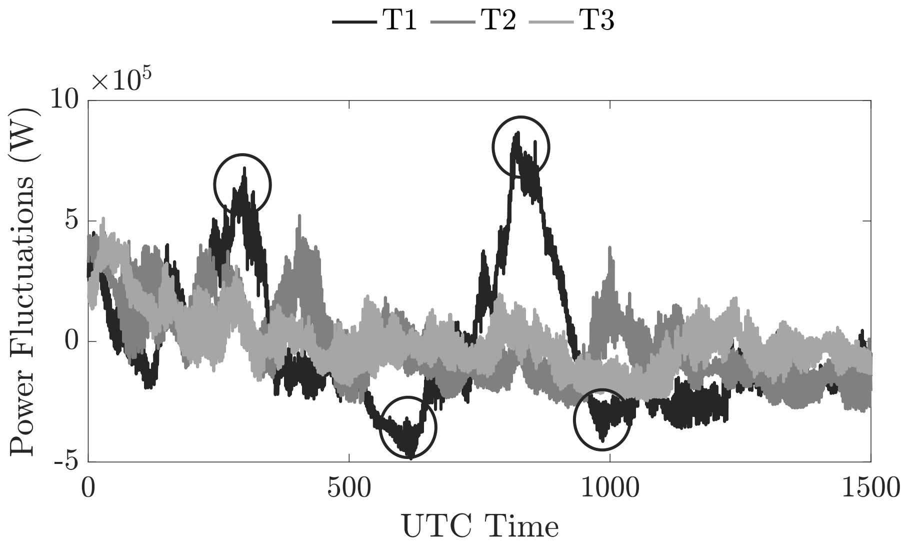

Figure 12. Power fluctuations of three turbines in a streamwise column during the AGW event. The black circles mark peaks and troughs of low-frequency oscillations in the power output of T1, which are associated with the presence of AGWs.

AGW inflow. These fluctuations are significantly attenuated for T2 and nearly disappear for T3. This trend results from the convective instability mechanism, which shifts the low-frequency velocity fluctuations in the inflow to higher-frequency ones in the wake region, as shown in the TKE spectra of the AGW case (top plot of Fig.8). Consequently, the inflow conditions for T2 and T3 feature fewer large-scale wind speed fluctuations.

However, it is noteworthy that T2 exhibits power peaks with lower magnitudes and a time delay of approximately 100 s compared to T1. Considering the advection velocity of the AGWs ($U_{\mathrm{hub}} = 5$ m/s) and the turbine spacing ($4D = 504$ m), these peaks could be caused by the AGW event. Specifically, T2 occasionally operates in large-scale AGW flow structures when the wake behind T1 meanders away, temporarily exposing T2 to the undisturbed AGW inflow.

4 Conclusions

By simulating turbine flow under an AGW event and a standard atmospheric boundary layer (non-AGW), we investigate the impact of AGWs on two key phenomena in wind turbine wake dynamics: wake meandering and wake turbulence generation. Additionally, we analyze mean wake recovery and turbine power fluctuations to support our findings.

Firstly, AGWs result in stronger low-frequency meandering motions in the wake region. This is attributed to two factors: (i) large-scale AGW flow structures generate low-frequency, large-magnitude velocity fluctuations in both the spanwise and vertical directions, amplifying wake meandering, and (ii) smaller-scale turbulent structures (with length scales greater than three rotor diameters) become more intense due to the elevated turbulence levels. The combination of stronger wake meandering and enhanced turbulent mixing in the instantaneous wake flow leads to faster mean wake recovery under AGW inflow conditions.

Secondly, TKE spectra in the wake region consistently peak at a Strouhal number of approximately 0.3 for both AGW and non-AGW cases, even though the dominant frequencies in the AGW inflow are significantly lower. This finding suggests that turbulence generation in the far-wake region adheres to the convective instability mechanism in both cases. Compared to the non-AGW case, the AGW case exhibits higher inflow TKE levels but a lower amplification factor via convective instabilities in the wake region, likely due to reduced wake shear resulting from faster wake recovery. To further support this conclusion, we examine the power production of three turbines arranged in a streamwise column under AGW inflow conditions. Large-scale AGW flow structures induce significant low-frequency power fluctuations at the most upstream turbine. However, these fluctuations are significantly attenuated at the two downstream turbines, which predominantly operate within the wake regions. This observation underscores the dominant role of convective instabilities in wake turbulence generation.

These findings offer insights for wake modeling under realistic atmospheric conditions, particularly in the presence of transient phenomena such as AGWs. Furthermore, the current measurement-driven LES method can serve as a robust tool for understanding and modeling the inter-scale coupling between mesoscale synoptic forcing and microscale wind-farm flow dynamics.

The present study focuses on terrain-induced AGWs, with a certain period which depends on the wavelength of the AGWs and their effective streamwise advection speed. In other synoptic situations, this period could vary significantly. Furthermore, AGWs can also be triggered by meteorological phenomena such as thunderstorms and cold or warm fronts. In such cases, AGWs can be propagating waves. Future study should incorporate AGW events originating from various sources and with different periods to comprehensively understand their roles in wake dynamics. Additionally, extending the measurement-driven LES method to other transient atmospheric phenomena, such as convective structures and low-level jets, represents a promising direction for further investigation.

Data availability. The atmospheric measurement data used in this paper are open source and can be found at https://a2e.energy.gov/data.

Author contributions. DF was responsible for the writing-original draft, conceptualization, methodology, software, validation, and formal analysis. SJW was responsible for the writing-review and editing, conceptualization, supervision, project administration, funding acquisition.

Competing interests. The authors declare that they have no conflict of interest.

https://doi.org/10.5194/wes-2025-52
Preprint. Discussion started: 8 April 2025

WIND ENERGY SCIENCE DISCUSSIONS

Acknowledgements. This work has been partially supported by the MERIDIONAL project, which receives funding from the European
255 Union's Horizon Europe Programme under the grant agreement No. 101084216.

https://doi.org/10.5194/wes-2025-52
Preprint. Discussion started: 8 April 2025

References

Ainslie, J. F.: Calculating the flowfield in the wake of wind turbines, Journal of wind engineering and Industrial Aerodynamics, 27, 213–224, 1988.

Allaerts, D., Quon, E., Draxl, C., and Churchfield, M.: Development of a time–height profile assimilation technique for large-eddy simulation, Boundary-Layer Meteorology, 176, 329–348, 2020.

Allaerts, D., Quon, E., and Churchfield, M.: Using observational mean-flow data to drive large-eddy simulations of a diurnal cycle at the SWiFT site, Wind Energy, 26, 469–492, 2023.

Churchfield, M. J., Lee, S., Michalakes, J., and Moriarty, P. J.: A numerical study of the effects of atmospheric and wake turbulence on wind turbine dynamics, Journal of turbulence, p. N14, 2012.

Deardorff, J. W.: Stratocumulus-capped mixed layers derived from a three-dimensional model, Boundary-layer meteorology, 18, 495–527, 1980.

Debnath, M., Scholbrock, A. K., Zalkind, D., Moriarty, P., Simley, E., Hamilton, N., Ivanov, C., Arthur, R. S., Barthelmie, R., Bodini, N., et al.: Design of the American Wake Experiment (AWAKEN) field campaign, in: Journal of Physics: Conference Series, vol. 2265, p. 022058, IOP Publishing, 2022.

Draxl, C., Worsnop, R. P., Xia, G., Pichugina, Y., Chand, D., Lundquist, J. K., Sharp, J., Wedam, G., Wilczak, J. M., and Berg, L. K.: Mountain waves can impact wind power generation, Wind Energy Science, 6, 45–60, 2021.

Durran, D. R.: Lee waves and mountain waves, Encyclopedia of atmospheric sciences, 1161, 1169, 2003.

Feng, D., Li, L. K., Gupta, V., and Wan, M.: Componentwise influence of upstream turbulence on the far-wake dynamics of wind turbines, Renewable Energy, 200, 1081–1091, 2022.

Feng, D., Gupta, V., Li, L. K., and Wan, M.: Parametric study of large-eddy simulation to capture scaling laws of velocity fluctuations in neutral atmospheric boundary layers, Physics of Fluids, 36, 2024a.

Feng, D., Gupta, V., Li, L. K., and Wan, M.: Resolvent analysis for predicting energetic structures in the far wake of a wind turbine, Physics of Fluids, 36, 2024b.

Foti, D., Yang, X., and Sotiropoulos, F.: Similarity of wake meandering for different wind turbine designs for different scales, Journal of Fluid Mechanics, 842, 5–25, 2018.

Heisel, M., Hong, J., and Guala, M.: The spectral signature of wind turbine wake meandering: A wind tunnel and field-scale study, Wind Energy, 21, 715–731, 2018.

Jonkman, J.: Definition of a 5-MW Reference Wind Turbine for Offshore System Development, National Renewable Energy Laboratory, 2009.

Larsen, G. C., Madsen, H. A., Thomsen, K., and Larsen, T. J.: Wake meandering: a pragmatic approach, Wind Energy: An International Journal for Progress and Applications in Wind Power Conversion Technology, 11, 377–395, 2008.

Moeng, C.-H.: A large-eddy-simulation model for the study of planetary boundary-layer turbulence, Journal of the Atmospheric Sciences, 41, 2052–2062, 1984.

Moriarty, P., Hamilton, N., Debnath, M., Herges, T., Isom, B., Lundquist, J. K., Maniaci, D., Naughton, B., Pauly, R., Roadman, J., et al.: American wake experiment (awaken), Tech. rep., Lawrence Livermore National Lab.(LLNL), Livermore, CA (United States . . . , 2020.

Nappo, C. J.: Mountain Waves, in: International Geophysics, vol. 102, pp. 57–85, Elsevier, 2012.

https://doi.org/10.5194/wes-2025-52
Preprint. Discussion started: 8 April 2025

Ollier, S. J. and Watson, S. J.: Modelling the impact of trapped lee waves on offshore wind farm power output, Wind Energy Science Discussions, 2022, 1–43, 2022.

Quon, E.: Measurement-driven large-eddy simulations of a diurnal cycle during a wake-steering field campaign, Wind Energy Science, 9, 495–518, 2024.

Skamarock, W. A., Klemp, J. B., Dudhia, J., Gill, D. O., Barker, D. M., Duda, M. G., Huang, X.-Y., Wang, W., and Power, J. G.: A Description of the Advanced Research WRF Version 3: NCAR Technical Note NCAR/TN-475+STR, Tech. rep., NCAR, Boulder, CO, https://opensky.ucar.edu/islandora/object/technotes%3A500/datastream/PDF/view, 2008.

Trujillo, J.-J., Bingöl, F., Larsen, G. C., Mann, J., and Kühn, M.: Light detection and ranging measurements of wake dynamics. Part II: two-dimensional scanning, Wind Energy, 14, 61–75, 2011.

Wilczak, J. M., Stoelinga, M., Berg, L. K., Sharp, J., Draxl, C., McCaffrey, K., Banta, R. M., Bianco, L., Djalalova, I., Lundquist, J. K., et al.: The second wind forecast improvement project (WFIP2): Observational field campaign, Bulletin of the American Meteorological Society, 100, 1701–1723, 2019.

Wise, A. S., Arthur, R. S., Abraham, A., Wharton, S., Krishnamurthy, R., Newsom, R., Hirth, B., Schroeder, J., Moriarty, P., and Chow, F. K.: Large-eddy simulation of an atmospheric bore and associated gravity wave effects on wind farm performance in the Southern Great Plains, Wind Energy Science Discussions, 2024, 1–35, 2024.

Wu, Y.-T. and Porté-Agel, F.: Large-eddy simulation of wind-turbine wakes: evaluation of turbine parametrisations, Boundary-layer meteorology, 138, 345–366, 2011.

Xia, G., Draxl, C., Raghavendra, A., and Lundquist, J. K.: Validating simulated mountain wave impacts on hub-height wind speed using SoDAR observations, Renewable Energy, 163, 2220–2230, 2021.